A non-oscillatory method for spallation studies

Shaoping Xiao*,†,‡

*Department of Mechanical and Industrial Engineering and Center for Computer-Aided Design,
3131 Seaman Center, The University of Iowa, Iowa City, IA 52242, U.S.A.*

SUMMARY

This paper introduces a non-oscillatory method, the finite element flux-corrected transport (FE-FCT) method for spallation studies. This method includes the implementation of a one-dimensional FCT algorithm into a total Lagrangian finite element method. Consequently, the FE-FCT method can efficiently eliminate fluctuations behind shock wave fronts without smearing them. In multidimensional simulations, the one-dimensional FCT algorithm is used on each grid line of the structured meshes to correct the corresponding component of nodal velocities separately. The requirement of structured meshes is satisfied by using an implicit function so that arbitrary boundaries of the simulated object can be described. In this paper, the proposed FE-FCT method is applied in spallation studies. One- and two-dimensional examples show this non-oscillatory method could be one of the candidates to accurately predict spallation and the spall thickness. Copyright © 2005 John Wiley & Sons, Ltd.

KEY WORDS: FE-FCT; implicit function; spallation; shock wave

1. INTRODUCTION

Spallation is an interesting component of dynamic fracture. Also known as spall, spall fracture, or by other names, this phenomenon occurs when waves, usually shock waves, interact to produce a region of tension in the interior of a material body. Therefore, the method that can precisely describe the shock wave propagation and interaction in solids will improve our understanding of material spallation mechanism under dynamic loads, such as impact and explosion. Numerical simulation has become a powerful tool to elucidate the complex mechanics and physics phenomena, including spallation. Some current numerical methods, however, demonstrate significant difficulties in modeling spallation due to fluctuations that are always observed behind shock wave fronts. As a result, development of non-oscillatory

---

*Correspondence to: Shaoping Xiao, Department of Mechanical and Industrial Engineering and Center for Computer-Aided Design, 3131 Seaman Center, The University of Iowa, Iowa City, IA 52242, U.S.A.
†E-mail: shaoping-xiao@uiowa.edu
‡Assistant Professor.

Copyright © 2005 John Wiley & Sons, Ltd.

methods, which can accurately describe the shock wave propagation and interaction in solids, for spallation studies has become a pertinent focus of research.

Finite difference methods have been used for wave propagation and spallation studies. Eftis *et al.* [1] implemented a viscoplastic material description in a finite difference wave propagation computer code to predict material damage and spall fracture under high strain-rate conditions. They introduced a scalar variable for the evolution of the material damage into the elasto-viscoplastic constitutive equations in order to describe rate-dependent, compressible, inelastic deformation and ductile fracture. Fortov and co-workers [2] developed a two-dimensional finite difference hydrodynamic elastoplastic code with the Lagrangian description to simulate the laser-induced spall phenomena. McLaughlin *et al.* [3] performed three-dimensional linear finite difference calculations to study the effects of the topographic bench on spalls. More recently, finite element methods [4] have been applied to simulate wave propagation and spallation. Fourney *et al.* [5] used a finite element method to study the fragmentation mechanism in carter blasting. They obtained the displacements of several points in the crater region which are in accord with the measured displacements. Finite element simulations have also been used to study the film spallation process induced by the pulsed laser peening [6]. In addition, molecular dynamics has recently been applied to analysis of the mechanical behaviour of materials, including spallation. Wagner *et al.* [7] showed that the spall strength was proportional to the logarithm of the applied strain rate when they examined both perfect crystals and granular solids by using molecular dynamics. Molecular dynamics simulations were also performed to study the effect of stress triaxiality on void growth in dynamic fracture of metals [8].

It is common to use the artificial bulk viscosity [9] in numerical simulations for shock wave propagation and spallation studies. The viscosity can efficiently reduce fluctuations behind shock wave fronts. However, one can observe that the wave fronts are smeared over several elements or several spacing steps, if finite element or finite difference methods are used, respectively. Furthermore, the viscosity can result in energy dissipation. Boris and Book [10, 11] proposed a flux-corrected transport (FCT) algorithm which has the capability to overcome the above issues. The FCT algorithm was first implemented into the finite difference methods [12]. Since the finite element methods have currently reached a mature state of development, the incorporation of the FCT algorithm with the finite element methods will be of significant potential benefit. Löhner and co-workers [13] combined the FCT algorithm with an Eulerian finite element method and obtained good results for Navier–Stokes equations. Georghiou *et al.* [14] developed a similar two-dimensional finite element-FCT method containing a low-order, positive, ripple-free scheme and a high-order scheme. This research has been principally conducted to study shocks in fluids. Zhang and co-workers [15] successfully combined the FCT algorithm with a Lagrangian finite element method and obtained some interesting results in one-dimensional transition problems.

In this paper, the author will introduce a new finite element flux-correction transport (FE-FCT) method for spallation studies of structures. In the proposed method, a fundamental FCT algorithm proposed by Boris and Book [10, 11] is implemented into a total Lagrangian finite element method with structured meshes. This one-dimensional FCT algorithm contains two stages: transport and anti-diffusion. Since meshes distort, corresponding to the deformation of structures under the Lagrangian description, there is no mass flow between elements. As a result, density flux vanishes in the developed FE-FCT method. Furthermore, only equations of motion are solved at the transport stage so that the FCT algorithm corrects only nodal velocities, i.e. nodal momenta during the simulation. The author [16] has used this method to study wave propagations in solids. Once structured meshes are generated, each component of

nodal velocities will be corrected independently within each time step along the corresponding mesh grid lines. According to the examples in Reference [16], this FE-FCT method can give accurate examples of shock wave propagation for both one- and two-dimensional problems. In other words, the FE-FCT method can efficiently eliminate fluctuations behind shock wave fronts while simultaneously maintaining shock wave fronts. However, the requirement of structured meshes for the implementation of the FCT algorithm in this FE-FCT method will prevent simulating objects with arbitrary boundaries, especially in multidimensional problems. The author introduces an implicit function, similar to the one used in the structured extended finite element method [17, 18], as well as the level set approach [19, 20], to describe boundaries of the simulated objects. This implicit function enables the FE-FCT method to model boundaries that are not coincident with the mesh. Since the FE-FCT method is advantageous in simulating shock wave propagations in solids, it will have the significant potential to study the spallation due to shock wave interacting. In this paper, the author will employ this non-oscillatory method in spallation studies. Several damage models will be introduced, and the computational results will be compared with the experimental data.

The outline of this paper is as follows. In Section 2, the general introduction of the FE-FCT method is given. It includes descriptions of the governing equations, the FCT algorithm and the implicit function. A one-dimensional example in Section 3 shows the FE-FCT method has the ability to accurately predict shock wave propagation and spallation. Several one- and two-dimensional spallation examples with various damage models are studied in Section 4, compared with the experimental data, and followed by the conclusions.

2. THE FE-FCT METHOD

2.1. Governing equations

The material (Lagrangian) form of momentum equations can be written as

$$\nabla_0 \cdot \mathbf{P} + \rho_0 \mathbf{b} = \rho_0 \ddot{\mathbf{u}} \quad \text{or} \quad \frac{\partial P_{ji}}{\partial X_j} + \rho_0 b_i = \rho_0 \ddot{u}_i \tag{1}$$

where ρ_0 is the initial density, $\mathbf{P}$ is the nominal stress tensor, $\mathbf{b}$ is the body force, $\mathbf{u}$ is the displacement, $\mathbf{X}$ are the material (Lagrangian) co-ordinates, and the superposed dots denote material time derivatives. Indices repeated twice in a term are summed in this paper. Equation (1) is formulated in the reference configuration Ω_0. The above form of the momentum equations can be written in a spatial form so that

$$\nabla \cdot \boldsymbol{\sigma} + \rho \mathbf{b} = \rho \ddot{\mathbf{u}} \quad \text{or} \quad \frac{\partial \sigma_{ji}}{\partial x_j} + \rho b_i = \rho \ddot{u}_i \tag{2}$$

where ρ is the current density, $\boldsymbol{\sigma}$ is the Cauchy stress, and $\mathbf{x}$ are the spatial (Eulerian) co-ordinates. By conservation of mass, there is

$$\rho J = \rho_0 \tag{3}$$

where J is the Jacobian determinant of deformation gradient $\mathbf{F}$, which are defined by

$$J = \det(\mathbf{F}) \quad F_{ij} = \frac{\partial x_i}{\partial X_j} \tag{4}$$

The two forms of momentum equations in (1) and (2) are equivalent and differ in form only because they are expressed in different descriptions; see Reference [21]. In this paper, the author will use a total Lagrangian finite element method to solve momentum equations of (1); and the FE approximation for the displacement field is

$$\mathbf{u}^h(\mathbf{X}, t) = \mathbf{N}^{\mathrm{T}}(\mathbf{X})\mathbf{u}(t) \quad \text{or} \quad u_i^h(\mathbf{X}, t) = N_J(\mathbf{X})u_{iJ}(t) \tag{5}$$

where the shape function $N_J(\mathbf{X})$ is a function of material co-ordinates in the total Lagrangian description, and $\mathbf{u}_J(t) = \mathbf{u}(\mathbf{X}_J, t)$ represent nodal displacements. The approximation for the first derivatives of the displacement, with respect to the material co-ordinates, can be written as

$$\nabla_0 \mathbf{u}^h(\mathbf{X}, t) = \mathbf{B}^{\mathrm{T}}(\mathbf{X})\mathbf{u}(t) \quad \text{or} \quad \frac{\partial u_i^h(\mathbf{X}, t)}{\partial X_j} = \frac{\partial N_J(\mathbf{X})}{\partial X_j} u_{iJ}(t) \tag{6}$$

The discrete momentum equation can be obtained by using the Galerkin weak form. In the reference configuration, the weak form of the linear momentum conservation equation (1) is

$$\int_{\Omega_0} \delta u_i \rho_0 \ddot{u}_i \, \mathrm{d}\Omega_0 = \int_{\Omega_0} \delta u_i \rho_0 b_i \, \mathrm{d}\Omega_0 - \int_{\Omega_0} \delta F_{ij} P_{ji} \, \mathrm{d}\Omega_0 + \int_{\Gamma_0^t} \delta u_i \bar{t}_i \, \mathrm{d}\Gamma_0^t \tag{7}$$

where δu_i is the test function, and $\bar{t}_i$ is the boundary traction on the traction boundary Γ_0^t. Substituting (5) and (6) into (7) and using a diagonal mass matrix, the discrete equations can be obtained as

$$\mathbf{M}\ddot{\mathbf{u}} = \mathbf{f}^{\mathrm{ext}} - \mathbf{f}^{\mathrm{int}} \quad \text{or} \quad M_I \ddot{u}_{iI} = f_{iI}^{\mathrm{ext}} - f_{iI}^{\mathrm{int}} \tag{8}$$

where M_I is the nodal mass of node I; and f_{iI}^{ext}, f_{iI}^{int} are the external and internal nodal forces, respectively, which are given by

$$f_{iI}^{\mathrm{ext}} = \int_{\Omega_0} \rho_0 N_I(\mathbf{X})b_i \, \mathrm{d}\Omega_0 + \int_{\Gamma_0^t} N_I(\mathbf{X})\bar{t}_i \, \mathrm{d}\Gamma_0^t \tag{9}$$

$$f_{iI}^{\mathrm{int}} = \int_{\Omega_0} \frac{\partial N_I(\mathbf{X})}{\partial X_j} P_{ji} \, \mathrm{d}\Omega_0 \tag{10}$$

2.2. Implementation of the flux-corrected transport algorithm

There are two stages in the FCT algorithm. One is the transport stage and the other is the anti-diffusion stage. The transport stage contains the time integration step to solve the discrete equations. The anti-diffusion stage is a corrective stage which corrects numerical errors introduced in the transport stage. Both stages are conservative and positive. Their interaction enables the FCT algorithm to treat discontinuities without the dispersively generated ripples (oscillations). The FCT algorithm was first developed for finite difference methods [10, 11] to

flawlessly solve shock wave propagation problems. As an instance of the usage of the FCT algorithm, the author considers a function U, which is a function of time and space in one dimension, in a finite element model with a regular mesh. The nodal value of function U at node j and time step $n + 1$ can be written as

$$U_j^{n+1} = U(X_j, t + \Delta t) = f(\mathbf{U}^n, \Delta t, \Delta X) \tag{11}$$

where Δt is the time-step size, ΔX is the mesh size, and $\mathbf{U}^n$ represents a vector of nodal values of the function at time t. If the function U has strong discontinuities, one can observe fluctuations around the discontinuities. Therefore, an additional treatment, such as the FCT algorithm, is needed to eliminate fluctuations. The general one-dimensional FCT algorithm [10] can be expressed as follows:

(a) Transport calculation: obtaining trial values of function U at time step $n + 1$ from (11)

$$\tilde{U}_j^{n+1} = f(\mathbf{U}^n, \Delta t, \Delta X) \tag{12}$$

(b) Diffusive flux calculations:

$$\varphi_j^0 = \eta_1 (U_{j+1}^n - U_j^n) \tag{13}$$

where η_1 is a diffusive coefficient.
(c) Diffusion:

$$\bar{U}_j^{n+1} = \tilde{U}_j^{n+1} + \varphi_j^0 - \varphi_{j-1}^0 \tag{14}$$

(d) Anti-diffusive flux calculations:

$$\varphi_j^1 = \eta_2 (\tilde{U}_{j+1}^n - \tilde{U}_j^n) \tag{15}$$

where η_2 is an anti-diffusive coefficient.
(e) Limitation of anti-diffusive fluxes:

$$\varphi_j^C = S \cdot \max\{0, \min[S \cdot \Delta_{j-1}, |\varphi_j^1|, S \cdot \Delta_{j+1}]\} \tag{16}$$

where $\Delta_{j-1} = \bar{U}_j^{n+1} - \bar{U}_{j-1}^{n+1}$, and $S = sign(\varphi_j^1)$.
(f) Anti-diffusion:

$$U_j^{n+1} = \bar{U}_j^{n+1} - \varphi_j^C + \varphi_{j-1}^C \tag{17}$$

In this paper, the diffusive coefficient and anti-diffusive coefficient are constant (i.e. $\eta_1 = \eta_2 = 0.125$ [10]); and the FCT algorithm is shown to be an efficient and accurate process [10, 11]. Since the FE-FCT method is under a Lagrangian description, there is no mass flow between elements. On the other hand, only the equations of motion are solved in the transport stage of the FCT algorithm. The discrete equations can be written as the following differential equations:

$$\dot{v}_{iI} = \frac{f_{iI}^{\text{ext}} - f_{iI}^{\text{int}}}{M_I} \tag{18}$$
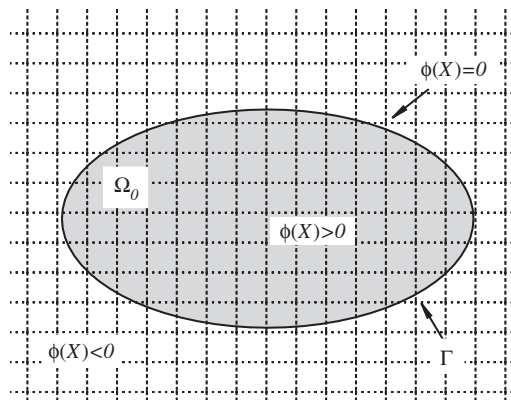
Figure 1. An object described by an implicit function under a structured mesh.

The author would like to note, here, that multidimensional FCT algorithms has been proposed by Zalesak [22] for fluids and been implemented into a two-dimensional finite element method for gas discharge problems [14]. However, since each component of the velocity is independently solved in multidimensional problems as shown in (18), the one-dimensional FCT algorithm can be used to correct nodal velocities, i.e. nodal momenta. The correction is applied along each grid line as long as structured meshes are provided. Generally, in a one-dimensional problem, the nodal velocities are corrected along the one-dimensional grid. In two-dimensional cases with two-dimensional quadrilateral meshes, horizontal and vertical grid lines occur in the reference configuration. After time integration of equations of motion at the transport stage, the FCT algorithm will correct the x components of nodal velocities along each horizontal grid line independently. Similarly, the y components of nodal velocities are corrected separately along each vertical grid line. Then, the calculations of displacements, strains, stresses and energy are based on the corrected nodal velocities.

2.3. Implementation of an implicit function

The FCT algorithm, described in the above, is easy to implement in finite element methods. However, such implementation requires regular meshes or structured meshes. The conventional finite element methods with structured meshes have difficulty solving multidimensional problems with arbitrary boundaries. Here, the author uses an implicit function [17, 18] to describe the arbitrary boundaries in the finite element methods. Figure 1 shows an object with body Ω_0 and boundary Γ under a structured mesh in the reference configuration. The simulated object can be described by an implicit function $\phi(\mathbf{X})$ so that

$$\phi(\mathbf{X}) = 0 \quad \text{on } \Gamma$$

$$\phi(\mathbf{X}) > 0 \quad \text{inside } \Omega_0 \tag{19}$$

$$\phi(\mathbf{X}) < 0 \quad \text{outside } \Omega_0$$

The implicit function can be initially chosen as a signed distance function or defined by radial basis functions from a set of points. Therefore, the weak form (7) can be rewritten as

$$\int_{\Omega_0} \delta u_i H(\phi) \rho_0 \ddot{u}_i \, \mathrm{d}\Omega_0 = \int_{\Omega_0} \delta u_i H(\phi) \rho_0 b_i \, \mathrm{d}\Omega_0$$

$$- \int_{\Omega_0} H(\phi) \delta F_{ij} P_{ji} \, \mathrm{d}\Omega_0 + \int_{\Gamma^t} \delta u_i \bar{t}_i \, \mathrm{d}\Gamma^t \tag{20}$$

where

$$H(\phi) = H(\phi(\mathbf{X})) = \begin{cases} 0 & \phi < 0 \\ 1 & \phi \geqslant 0 \end{cases} \tag{21}$$

Then, (9) and (10) for nodal forces can be rewritten as

$$f_{iI}^{\text{ext}} = \int_{\Omega_0} \rho_0 H(\phi) N_I(\mathbf{X}) b_i \, \mathrm{d}\Omega_0 + \int_{\Gamma^t} N_I(\mathbf{X}) \bar{t}_i \, \mathrm{d}\Gamma^t \tag{22}$$

$$f_{iI}^{\text{int}} = \int_{\Omega_0} H(\phi) \frac{\partial N_I(\mathbf{X})}{\partial X_j} P_{ji} \, \mathrm{d}\Omega_0 \tag{23}$$

The above equation shows that only part of an element, which is crossed by the boundary, contributes to Ω_0. Therefore, the integration procedure is more involved. A simple way [17] to perform the integrations in (22) and (23) is to cut each element into several subelements by the boundary. Then, the quadratures over the element consist of the quadratures over those subelements. The integration on the traction boundary involves quadratures over the zero isobar of the FE approximated implicit function. The details can be found in References [17, 18].

2.4. Flowchart of the FE-FCT method

In short, the flowchart for the FE-FCT method can be written as follows:

(a) Generate a structured mesh and set initial values of material state variables.
(b) Construct an implicit function to describe the boundaries.
(c) Calculate nodal forces as (22) and (23).
(d) Obtain trial velocities: $\tilde{v}_{iI}^{n+1} = v_{iI}^n + ((f_{iI}^{\text{ext}} - f_{iI}^{\text{int}})/M_I)\Delta t$.
(e) Calculate diffusive fluxes: $\psi_{iI}^0 = \eta_1(v_{iI+1}^n - v_{iI}^n)$.
(f) Diffuse: $\bar{v}_{iI}^{n+1} = \tilde{v}_{iI}^{n+1} + \psi_{iI}^0 - \psi_{iI-1}^0$.
(g) Calculate anti-diffusive fluxes: $\psi_{iI}^1 = \eta_2(\tilde{v}_{iI+1}^n - \tilde{v}_{iI}^n)$.
(h) Apply limitation of anti-diffusive fluxes:

$$\psi_{iI}^C = S \cdot \max\{0, \min[S \cdot \Delta_{iI-1}, |\psi_{iI}^1|, S \cdot \Delta_{iI+1}]\}$$

where $\Delta_{iI-1} = \bar{v}_{iI}^{n+1} - \bar{v}_{iI-1}^{n+1}$, and $S = sign(\psi_{iI}^1)$.
(i) Anti-diffuse: $v_{iI}^{n+1} = \bar{v}_{iI}^{n+1} - \psi_{iI}^C + \psi_{iI-1}^C$.

(j) Update displacements and apply boundary conditions.

(k) Calculate strains and stresses.

(1) Output; if simulation is not complete, go to (c).

During the calculation of flux, diffusing, and anti-diffusing, node $I + 1$ or $I - 1$ are the neighbour nodes of node I on the same grid line. Fluxes ψ_{iI} one calculated for the ith component of nodal velocities along each grid line that is parallel to i (x or y) axis.

3. ADVANTAGES OF THE FE-FCT METHOD FOR SPALLATION SIMULATIONS

The FCT algorithm was first implemented in finite difference methods. Finite difference FCT methods have been widely used to model shock wave propagation in fluids [13, 14]. The FCT algorithm contains two stages: the transport stage and the anti-diffusion stage. Since the governing equations in finite difference methods, solved in the transport stage, contain a number of differential equations, multiple fluxes need to be corrected at the anti-diffusion stage of the FCT algorithm. When using finite element methods in solids, however, the discrete equations of motion are the only type of differential equations that must be solved at the transport stage of the FCT algorithm. Moreover, the Lagrangian finite element method is used, so that there is no mass flow between elements, i.e. no density flux in this model. Therefore, the FCT algorithm is used to correct only nodal velocities, i.e. nodal momenta. Consequently, once the structured meshes have been generated, each component of the nodal velocities is corrected separately within each time step along the grid lines. The one-dimensional FCT algorithm used in the paper is a fundamental scheme proposed by Boris and Book [10, 11], which, unlike other methods [14], does not require low-order and high-order schemes. The implementation of the FCT algorithm in the proposed FE-FCT method is therefore simpler than those used in most finite difference methods, and the FE-FCT method has been proven to be efficient for studying wave propagations in solids [16]. The following example will demonstrate the advantages of FE-FCT method on spall prediction and spall-thickness calculation.

Figure 2 illustrates a one-dimensional rod subjected to a triangular compressive pulse. The length of the rod is $L = 1.0\,\text{m}$. The pulse is with $\sigma_0 = 5000.0\,\text{N/m}^2$ and $t_0 = 0.05\,\text{s}$. The material properties of the rod are Young's modulus $E = 10\,000.0\,\text{N/m}^2$ and the density $\rho_0 = 100\,\text{Kg/m}^3$. One thousand elements are used in this example.
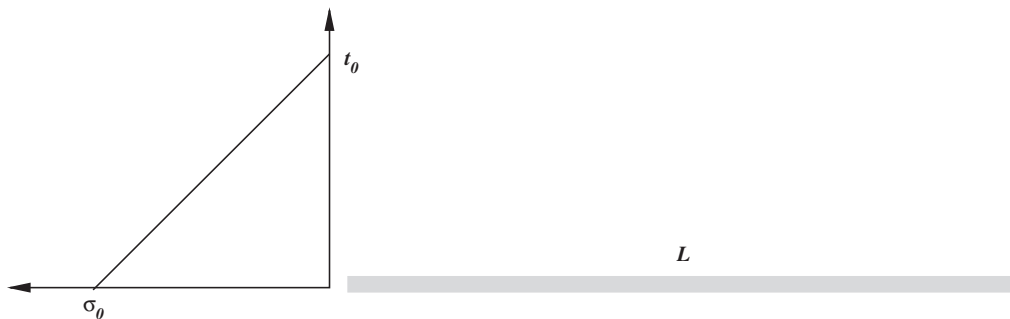

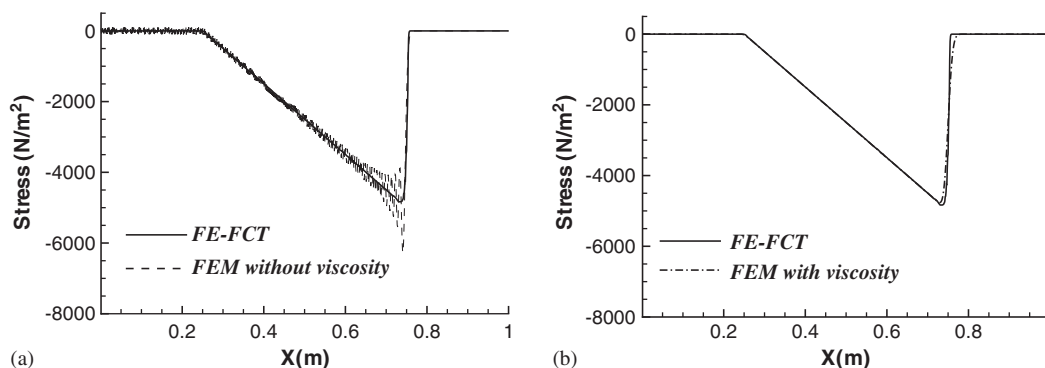Figure 2. An elastic rod with a triangular compressive pulse load.

Figure 3. The configurations of stress wave at $t = 0.075\,\text{s}$ using the FE-FCT method compared with: (a) the FEM without viscosity; and (b) the FEM with viscosity.

Table I. Comparison of the spallation prediction and spall thicknesses.

Spall stress	Theoretical analysis	The FE-FCT method	The FEM with viscosity	The FEM without viscosity
5500 Pa	No spallation	No spallation	No spallation	0.152 m
4500 Pa	0.225 m	0.226 m	0.230 m	0.201 m
2000 Pa	0.1 m	0.101 m	0.106 m	0.04 m

A compressive stress wave begins to propagate once the pulse is loaded. Figure 3 shows the stress wave calculated by the FE-FCT method, compared with the results of the finite element method (FEM) with or without viscosity. Figure 3(a) shows that the FE-FCT method can efficiently eliminate fluctuations behind the shock wave front normally observed when employing the finite element method without viscosity. Although the bulk viscosity can also eliminate the fluctuations, the shock wave front is smeared over several elements, as shown in Figure 3(b). This non-physical phenomenon will result in a blurred description of shock wave propagation and interaction. Another disadvantage of bulk viscosity is that system energy dissipates as discussed in Reference [16]. In contrast, the FE-FCT method can retain the strong discontinuity of the shock wave front as well as maintain conservation of energy [16].

In this demonstration, the reflection of the compressive stress wave at the free end of the rod generates a tensile stress wave. We assume that spallation occurs when the reflected tensile stress is beyond the spall stress. Such a simple spall criterion is only used for the purpose of demonstrating the advantages of FE-FCT application in this paper, however. Various void nucleation and growth models for spallation studies will be introduced in the next section. Table I presents spall thicknesses, which are calculated by using the FE-FCT method, compared with the ones from the theoretical analysis and finite element methods with or without viscosity. The theoretical analysis was performed by solving a wave equation. Various spall stresses are considered during the comparison. Based on the theoretical analysis, defining a spall stress of $\sigma_s = 5500\,\text{N/m}^2$, which is larger than the peak stress of the fully reflected tensile stress
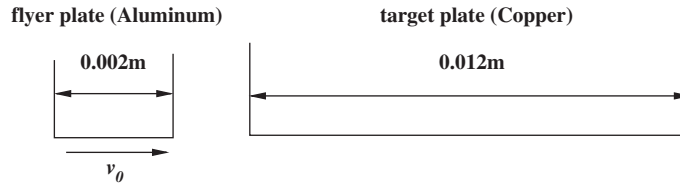
flyer plate (Aluminum)　　　　**target plate (Copper)**

0.002m　　　　　　　　　　　　**0.012m**

v_0

Figure 4. A flyer plate impacts a target plate (a one-dimensional model).

Table II. Material properties of aluminium and copper.

	Density $\rho_0(\mathrm{Kg/m}^3)$	Young's modulus $E(\mathrm{GPa})$	Poisson's ratio v
Aluminum	2785	100	0.33
Copper	8930	170	0.35

wave, results in no occurrence of spallation. The same prediction is obtained from the FE-FCT method as well as the finite element method with viscosity. However, the finite element method without viscosity predicts that spallation will occur, due to fluctuations of the peak stress beyond the spall stress. This example is illustrated in Figure 3(a). For low spall stresses, the spall thicknesses predicted by the FE-FCT method are very close to the theoretical results. The FE-FCT results are better than those predicted using the finite element method with viscosity, and much better than those obtained from the finite element method without viscosity. Therefore, the FE-FCT method demonstrates significant advantage for spallation analysis.

4. EXAMPLES

4.1. A one-dimensional spallation simulation with the DFRACT damage model

A one-dimensional FE-FCT model is used to simulate impact-driven spallation as shown in Figure 4. A flyer plate of aluminium with the velocity of $v_0 = 450\,\mathrm{m/s}$ impacts a target plate of copper. In this one-dimensional finite element model, there are 1200 elements in the target plate and 200 elements in the flyer plate. The material properties of aluminum and copper are listed in Table II. The condition of impenetrability [21] is used here to check if the flyer and the target are in contact or separated.

A ductile fracture model, called DFRACT [23], is used to deal with the processes of nucleation and growth of a large number of microvoids. This model includes nucleation and growth based on microphysical models, and it also describes the effect of growing damage on the stress–strain relations. The effective shear modulus, G_{eff}, and the yield strength, Y, can be calculated as

$$G_{\mathrm{eff}} = G\left[1 - \frac{15(1-v)}{7-5v}V_{\mathrm{V}}\right] \quad Y = E(1 - 4V_{\mathrm{V}}) \tag{24}$$
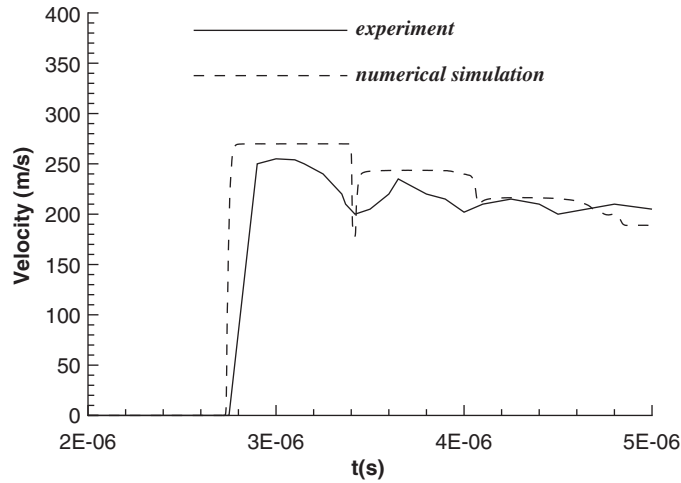
Figure 5. Comparison of the free-surface velocity profile.

where V_V is the void volume fraction. It is computed using the following formula:

$$V_V = V_{V0} + \Delta V_{VN} + \Delta V_{VG} \tag{25}$$

where V_{V0} is the initial void volume fraction; ΔV_{VN} and ΔV_{VG} are the increases in void volume fraction due to nucleation and growth, respectively.

New voids are generated when the tensile pressure P_S exceeds the nucleation threshold P_{N0} of the material. The pressure is calculated using the equation of motion [24]. On the other hand, the existing voids grow if the tensile pressure exceeds the growth threshold P_{G0} of the material. In the DFRACT model, the increases in nucleation and growth of voids, during a single time step, Δt, can be written as follows:

$$\Delta V_{VN} = 8\pi \dot{N}_0 e^{(P_S - P_{N0})/P_1} R_n^3 \Delta t, \quad \Delta V_{VG} = V_{V0}(e^{3/4[(P_S - P_{G0})/\eta]\Delta t} - 1) \tag{26}$$

where the material parameters of the DFRACT model for copper are

$$\dot{N}_0 = 2.8 \times 10^{18}\,\mathrm{m}^{-3}/\mathrm{s}, \quad P_{N0} = 5.0 \times 10^8\,\mathrm{N/m^2}, \quad P_1 = 2.0 \times 10^8\,\mathrm{N/m^2}$$

$$R_n = 1.0 \times 10^{-6}\,\mathrm{m}, \quad P_{G0} = 5.0 \times 10^8\,\mathrm{N/m^2}, \quad \eta = 7.5\,\mathrm{N\,s/m^2}$$

The free-surface velocity profile is shown in Figure 5. The spall thicknesses are 1.26 and 1.3 mm computed from the void volume fraction and the period of the oscillations in free-surface velocity profile, respectively. Both of them match fairly well with the experimental value, 1.15 mm, which is indicated in Reference [25].

4.2. A two-dimensional spallation simulation with the VG damage model

A two-dimensional FE-FCT model, shown in Figure 6, is used to study a problem similar to the previous one. The dimensions are $H_1 = 0.0004$ m, $H_2 = 0.0027$ m, and $L = 0.0012$ m. The
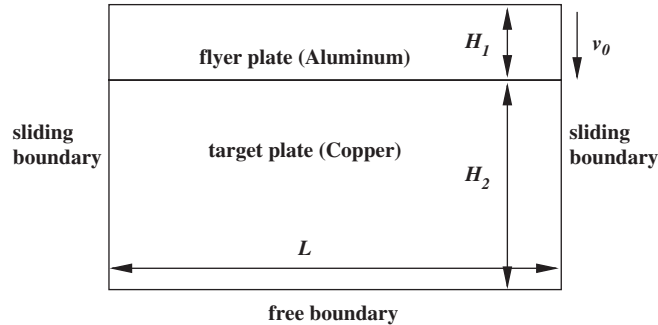
Figure 6. A flyer plate impacts a target plate (a two-dimensional model).

aluminium flyer has the impact velocity, $v_0 = 660 \, \text{m/s}$. The material properties are given in Table II. Plane strain is assumed here; 60 000 elements are used in the simulation.

The void-growth (VG) model [26] is used, and the presence of voids is expressed in terms of the distension ratio α. The porosity D is related to the distension ratio through the expression $D = 1 - 1/\alpha$. Then, the effective Young's modulus can be written as $E_{\text{eff}} = E(1 - D)$. The rate of change of α for copper is given by

$$\dot{\alpha} = \begin{cases} 0 & \Delta P \geqslant 0 \\ -\dfrac{(\alpha_0 - 1)^{2/3}}{\eta} \alpha (\alpha - 1)^{1/3} \Delta P & \Delta P < 0 \end{cases} \tag{27}$$

where η is a material parameter and it is $1.0 \, \text{N s/m}^2$ for copper. α_0 provides the initial distension to get the void growth start and it is set to be 1.0003 for the copper. ΔP is the driving stress for void growth and it is given by

$$\Delta P = \bar{P} - \frac{P_{\text{S}}}{\alpha} \ln \left(\frac{\alpha}{\alpha - 1} \right) \tag{28}$$

where $P_{\text{S}} = 0.17 \times 10^9 \, \text{N/m}^2$ is the threshold for void growth and $\bar{P}$ is the average mean stress in the porous region containing voids.

Figure 7 shows the evolutions of the free-surface velocity of the target. It is evident that the FE-FCT method can give non-oscillatory results for the free-surface velocity profile during spallation, unlike that of the FE method without viscosity. The configuration of the porosity is shown in Figure 8 and the calculated spall thickness is 0.232 mm. This outcome is in good agreement with the experimental result [25], 0.23 mm.

4.3. A plate with a central hole undergoing explosion

We consider a copper plate with a central hole whose radius is 0.00025 m. The plate undergoes explosion, as shown in Figure 9. Only one quarter of the plate is modelled with $L = 0.005$ m. The structured mesh (quadrilateral mesh) is generated for the problem. An implicit function is used to describe the boundary along the hole. One can see that the boundary cuts the elements, which are crossed by the boundary, into several subelements for integration. An example of this
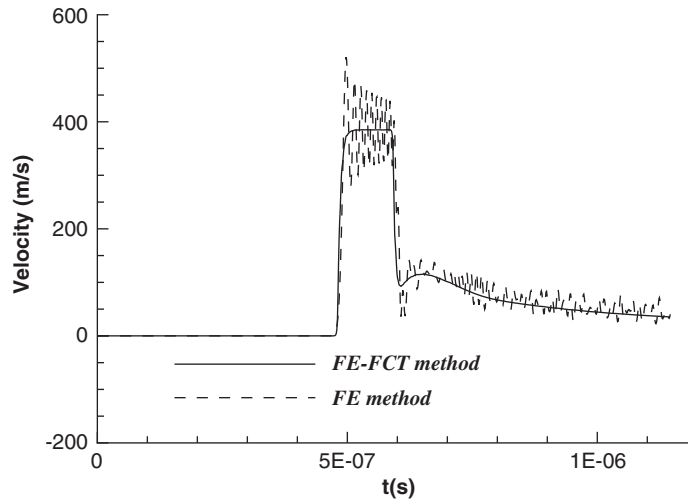
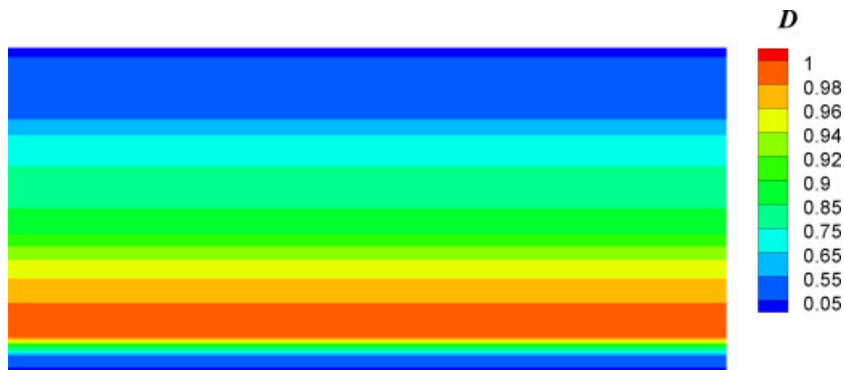Figure 7. Free-surface velocity profiles.

Figure 8. Configuration of the porosity.

cutting and crossing can be found in Figure 10. A velocity pulse, described by an exponential function here, is used to model the explosion loaded along the inner cycle of the hole. It is expressed as

$$v = v_0 e^{-\beta t} \tag{29}$$

where $v_0 = 1000.0 \, \text{m/s}$ and $\beta = 0.15e7 \, \text{s}^{-1}$.

The material properties of copper can be obtained from Table II. Once the explosion occurs, cylindrical waves will propagate in the plate as compressible stress waves. These waves will be reflected by the free boundaries and become tensile stress waves. Figure 11 shows average mean stress waves at $t_1 = 1.15 \, \mu\text{s}$ and $t_2 = 1.38 \, \mu\text{s}$. At time of $t_1 = 1.15 \, \mu\text{s}$, two sets of tensile
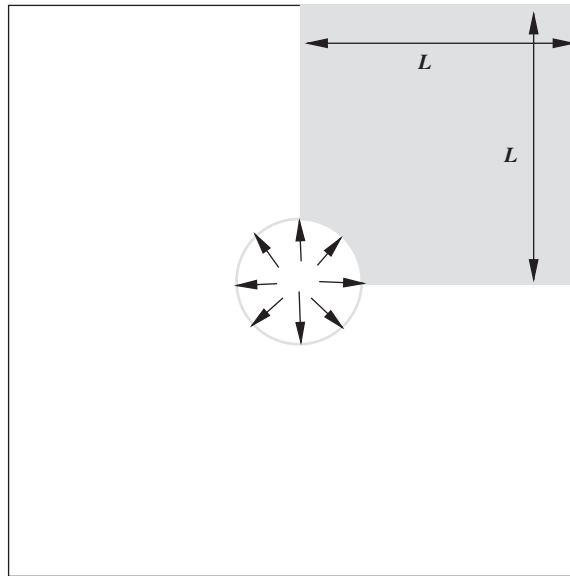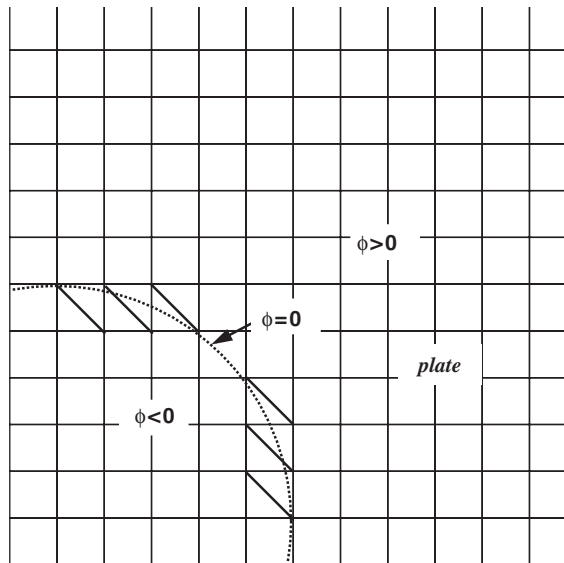
Figure 9. A plate with a central hole under explosion.

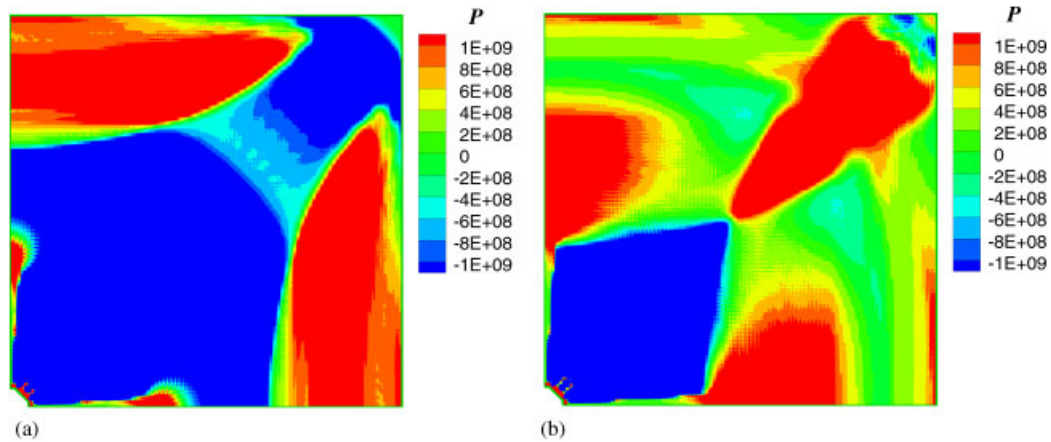Figure 10. Structured mesh for the plate with a hole.

Figure 11. Evolution of stress waves by the FE-FCT method: (a) $t_1 = 1.15\,\mu s$; and (b) $t_2 = 1.38\,\mu s$.
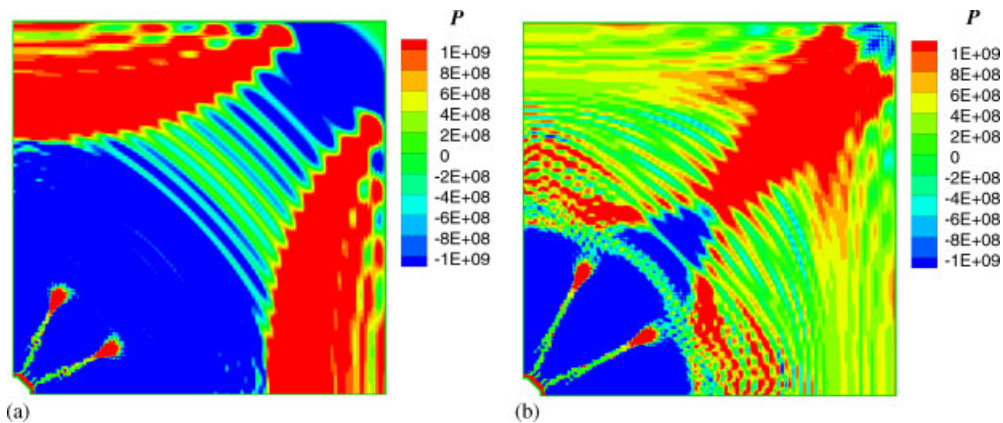

Figure 12. Evolution of stress waves by the FE method: (a) $t_1 = 1.15\,\mu s$; and (b) $t_2 = 1.38\,\mu s$.

stress waves occur after the wave reflections, and they interact with each other as shown in Figure 11(b). The evolution of stress waves for finite element simulation is shown in Figure 12. It is difficult to distinguish waves due to the fluctuations, especially when the wave interaction occurs. It is evident that the FE-FCT method can give accurate examples for shock wave propagations and interactions.

We use the VG model to describe the evolution of nucleation and growth of voids in this example. Figure 13 shows the evolution of the porosity. Once the reflected tensile stress waves interact with each other, the accumulated magnitude of the tensile stresses will result in void nucleation and growth. Then, the phenomenon of radial fracture can be observed as shown in Figure 13.
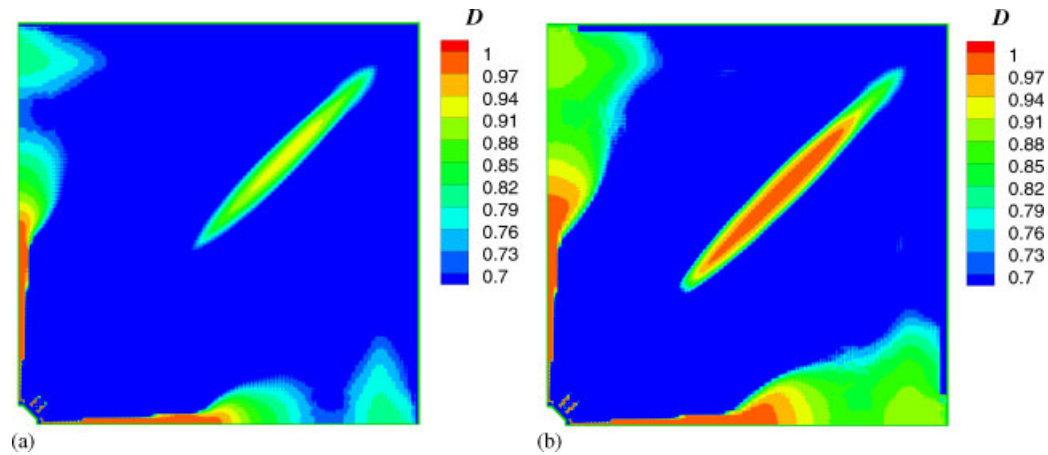
Figure 13. Evolution of porosity: (a) $t_1 = 1.5\,\mu s$; and (b) $t_2 = 1.7\,\mu s$.

5. CONCLUSIONS

Understanding shock wave propagation and interaction is key to spallation studies. Some numerical methods use artificial viscosity to eliminate the oscillations behind shock wave fronts. However, it smears the shock wave fronts and dissipates system energy. The incorporation of the flux-corrected transport (FCT) algorithm in Lagrangian finite element (FE) methods has significant potential due to the great versatility of finite element methods. Since only nodal velocities are updated through the time integration of discrete equations at the transport stage, the FCT algorithm corrects only nodal velocities, i.e. nodal momenta, in the proposed FE-FCT method. In multi-dimensional shock wave propagation problems, each component of nodal velocities can be corrected separately along the corresponding grid lines if structured meshes are constructed. The increment of CPU time due to the FCT algorithm is not a big issue, especially in multidimensional problems, since the one-dimensional FCT algorithm is employed. Such implementation of the one-dimensional FCT algorithm is simple and has been shown to be efficient for the accurate description of the shock wave propagation. However, the FCT approach used in this paper requires structured meshes. An implicit function is introduced to describe the arbitrary boundaries of objects. Therefore, the proposed FE-FCT method has a great deal of potential to solve multidimensional wave propagation and interaction problems. A one-dimensional example showed that the FE-FCT method predicts better spallation phenomena and spall thicknesses than the finite element method with or without artificial viscosity. We also studied several one- and two-dimensional examples to show that the results of the FE-FCT method are in good agreements with experimental results.

REFERENCES

1. Eftis J, Nemes JA, Randles PW. Viscoplastic analysis of plate-impact spallation. *International Journal of Plasticity* 1991; **7**(1–2):15–39.
2. Fortov VE, Kostin VV, Eliezer S. Spallation of metals under laser irradiation. *Journal of Applied Physics* 1991; **70**(8):4524–4531.
3. McLaughlin KL, Bonner JL, Barker T. Seismic source mechanisms for quarry blasts: modelling observed Rayleigh and Love wave radiation patterns from a Texas quarry. *Geophysical Journal International* 2004; **156**(1):79–93.
4. Hughes TJR. *The Finite Element Method*: *Linear Static and Dynamic Analysis*. Prentice-Hall/Dover: New York, 1987.
5. Fourney WL, Dick RD, Wang XJ, Wei Y. Fragmentation mechanism in crater blasting. *International Journal of Rock Mechanics and Mining Science and Geomechanics Abstracts* 1993; **30**(4):413–429.
6. Zhou M, Zeng DY, Kan JP, Zhang YK, Cai L, Shen ZH, Zhang XR, Zhang SY. Finite element simulation of the film spallation process induced by the pulsed laser peening. *Journal of Applied Physics* 2003; **94**(5):2968–2975.
7. Wagner NJ, Holian BL, Voter AF. Molecular-dynamics simulations of a 2-dimensional materials at high-strain rates. *Physical Review A* 1992; **45**(12):8457–8470.
8. Seppala ET, Belak J, Rudd RE. Effect of stress triaxiality on void growth in dynamic fracture of metals: a molecular dynamics study. *Physical Review B* 2004; **69**(13):Art. No. 134101.
9. Zukas JA. *High Velocity Impact Dynamics*. Wiley: New York, 1990.
10. Boris JP, Book DL. Flux-corrected transport 1. SHASTA, a fluid transport algorithm that works. *Journal of Computational Physics* 1973; **11**:38–69.
11. Book DL, Boris JP, Hain K. Flux-corrected transport 2. Generalizations of the method. *Journal of Computational Physics* 1975; **18**:248–283.
12. Yang DH, Liu E, Zhang ZJ, Teng J. Finite-difference modelling in two-dimensional anisotropic media using a flux-corrected transport technique. *Geophysical Journal International* 2002; **148**(2):320–328.
13. Löhner R, Morgan K, Peraire J, Vahdati M. Finite element flux-corrected transport (FEM-FCT) for the Euler and Navier–Stokes equations. *International Journal for Numerical Methods in Fluids* 1987; **7**(10):1093–1109.
14. Georghiou GE, Morrow R, Metaxas AC. A two-dimensional, finite-element, flux-corrected transport algorithm for the solution of gas discharge problems. *Journal of Physics D—Applied Physics* 2000; **33**(19):2453–2466.
15. Zhang JH, Duan ZP, Ding J. Simulating shock to detonation transition: algorithm and results. *Journal of Computational Physics* 1999; **150**(1):128–142.
16. Xiao SP. A FE-FCT method with implicit functions for the study of shock wave propagation in solids. *Wave Motion* 2004; **40**:263–276.
17. Belytschko T, Parimi C, Moës N, Sukumar N, Usui S. Structured extended finite element methods for solids defined by implicit surfaces. *International Journal for Numerical Methods in Engineering* 2003; **56**(4): 609–635.
18. Belytschko T, Xiao SP, Parimi C. Topology optimization with implicit functions and regularization. *International Journal for Numerical Methods in Engineering* 2003; **57**(8):1177–1196.
19. Cheng LT, Burchard P, Merriman B, Osher S. Motion of curves constrained on surfaces using a level-set approach. *Journal of Computational Physics* 2002; **175**:604–644.
20. Burchard P, Cheng LT, Merriman B, Osher S. Motion of curves in three spatial dimensions using a level-set approach. *Journal of Computational Physics* 2001; **170**:720–741.
21. Belytschko T, Liu WK, Moran B. *Nonlinear Finite Elements for Continua and Structures*. Wiley: New York, 2001.
22. Zalesak ST. Fully multidimensional flux-corrected transport algorithm for fluids. *Journal of Computational Physics* 1979; **31**:335–362.
23. Curran DR, Seaman L. Dynamic failure of solids. *Physics Reports—Review Section of Physics Letters* 1987; **147**(5–6):253–388.
24. Eliezer S, Ghatak A, Hora H, Teller E. *An Introduction to Equation of State*, *Theory and Applications*. Cambridge University Press: Cambridge, MA, 1986.
25. Ikkurthi VR, Chaturvedi S. Use of different damage models for simulating impact-driven spallation in metal plates. *International Journal of Impact Engineering* 2004; **30**:275–301.
26. Johnson JN, Gray III GT, Bourne NK. Effect of pulse duration and strain rate on incipient spall fracture in copper. *Journal of Applied Physics* 1999; **86**(9):4892–4901.